RSC Advances

PAPER

View Article Online
View Journal | View Issue



Cite this: *RSC Adv.*, 2026, **16**, 21465

# Fe-substituted $Na_{3.5}V_{1.5}Mn_{0.5}(PO_4)_3$ NaSICON cathode with multi-electron reactions and improved energy output

Loubna Chayal,[a] Soraia El Moutchou,[b] Noha Sabi,[b] Hicham Ben Youcef,[b] Hasna Aziam,*[b] Mohamed Saadi[a] and Mohammed Hadouchi*[a]

Sodium-ion batteries have emerged as a promising alternative to conventional lithium-ion batteries due to the abundance and low cost of sodium resources. NaSICON-based materials represent a highly competitive class of cathodes for sodium-ion batteries. Engineering NaSICON-type cathodes through rational design is a compelling approach to enhancing the overall energy density of sodium storage systems. In this study, the known $Na_{3.5}V_{1.5}Mn_{0.5}(PO_4)_3$ phase was strategically modified by partially substituting Mn with Fe using a Pechini route, followed by an *ex situ* carbon coating, leading to the formation of a novel ternary NaSICON-type $Na_{3.5}V_{1.5}Mn_{0.25}Fe_{0.25}(PO_4)_3$/C (NVMFP/C) cathode with enhanced properties. Structural and morphological analyses confirmed the high crystallinity and phase purity of the designed material (NVMFP/C). Electrochemical evaluation *versus* $Na^+/Na$ demonstrated a reversible capacity of 167 mA h $g^{-1}$ (~0.30 mA h $cm^{-2}$) at 0.1C, outstanding rate capability, and a high energy density of 412 Wh $kg^{-1}$ at 1C. Furthermore, the material exhibited remarkable cycling stability, with 74% capacity retention after 1400 cycles at 10C within the 1.5–4.3 V potential window. This promising electrochemical performance is attributed to the fast $Na^+$ diffusion kinetics, as confirmed by the galvanostatic intermittent titration technique (GITT), and the structural stabilization, resulting from this compositional engineering. Moreover, the synergy between the Pechini route, *ex situ* carbon coating, and Fe incorporation activates multiple redox reactions and enables the designed cathode to operate within an expanded potential range with significant capacitive contribution, providing a robust pathway toward high-energy-density sodium-ion batteries.

Received 16th January 2026
Accepted 17th April 2026

DOI: 10.1039/d6ra00418k

rsc.li/rsc-advances



## 1. Introduction

The growing demand for energy storage systems, driven by continuous technological progress, has substantially increased the consumption of critical raw materials required for their fabrication.[1–3] Among these systems, lithium-ion batteries (LIBs) currently dominate the market. However, the scarcity of lithium and its uneven geographic distribution pose challenges to long-term sustainability, highlighting the urgent need for alternative materials.[3–5] In this context, sodium has attracted considerable attention due to its natural abundance and low cost, positioning sodium-ion batteries (SIBs) as a promising replacement for LIBs. Importantly, SIBs operate through a "rocking-chair" mechanism similar to that of LIBs, enabling comparable working principles while offering a more resource-sustainable pathway.[6,7]

Since the appearance of SIBs, enormous amounts of effort have been deployed to develop new components for them, especially cathode materials, which are key determinants of the battery's total electrochemical capacity.[8,9] The employment of a high-voltage and large-capacity cathode material promotes the energy density and facilitates the practical application of SIBs.[10] Cathode materials for SIBs fall mainly into four categories: organic compounds, Prussian blue analogs, transition metal oxides, and polyanionic compounds.[11] Among these, NaSICON-phosphate, which belongs to the polyanionic compounds, has received great attention due to its robust framework resulting from stable P–O covalent bonds that provide crucial structural stability and generate spacious 3D interstices.[12–16] While developing high-capacity cathode materials is essential, the overall performance and safety of sodium-ion batteries also depend on the electrolyte system. Recent advances in supramolecular gel electrolytes (SGEs) have shown that self-assembled network structures can significantly improve ion transport and mechanical stability.[17] Combining such innovative electrolyte strategies with robust NaSICON-type frameworks could lead to

[a]*Laboratoire de Chimie Appliquée des Matériaux, Centre des Sciences des Matériaux, Faculty of Science, Mohammed V University in Rabat, Avenue Ibn Battouta, Rabat, BP 1014, Morocco. E-mail: m.hadouchi@um5r.ac.ma*

[b]*High Throughput Multidisciplinary Research (HTMR), College of Chemical Sciences and Engineering (CCSE), Mohammed VI Polytechnic University (UM6P), Lot 660 Hay Moulay Rachid, Ben Guerir, 43150, Morocco. E-mail: Hasna.AZIAM@um6p.ma*

the next generation of safe and high-energy-density storage devices.

In recent decades, the phosphate $Na_3V_2(PO_4)_3$ (NVP) has been extensively studied as a cathode for sodium-ion batteries due to its relatively high operating voltage (~3.4 V) and remarkable structural stability. Nevertheless, the practical application of this compound is limited by various factors, including its unsatisfactory capacity and energy density, as well as the toxicity of vanadium.[7] To address these limitations, various strategies have been employed, including the substitution of vanadium with low-cost and eco-friendly cations (*e.g.*, Fe and Mn),[18,19] carbon coating[20] and nanosizing.[21] In fact, metal cation doping is considered one of the most effective approaches to enhance the electrochemical performance of NVP.[22]

Recently, $Na_{3+x}V_{2-x}Mn_x(PO_4)_3$ (NVMP) has been extensively investigated as a cathode material for SIBs, especially the $Na_{3.5}V_{1.5}Mn_{0.5}(PO_4)_3$ NaSICON, driven by the low cost of Mn and its ability to enhance the operating voltage owing to the high voltage (3.6 V) of the $Mn^{2+}/Mn^{3+}$ couple compared to that of the $V^{3+}/V^{4+}$ couple (3.4 V).[10,23–27] Indeed, the substitution of $V^{3+}$ with $Mn^{2+}$ ion in NVP material enhances performance by increasing the charge carrier concentration and enlarging the lattice volume, which significantly facilitates the rapid diffusion of sodium ions.[28] Additionally, the synergistic effect of the $V^{3+}/V^{4+}$, $V^{4+}/V^{5+}$, and $Mn^{2+}/Mn^{3+}$ multi-electron reactions enables the appearance of three distinct voltage plateaus at 3.3, 3.6, and 3.9 V upon extending the cut-off voltage to 4.3 V.[29] Specifically, it has been shown that incorporating manganese at a content of up to $x = 0.25$ into NVMP triggers a beneficial $V^{4+}/V^{5+}$ redox reaction at 4.0 V and enhances the material's capacity, which ultimately improves the operating voltage and energy density of the material.[10] However, due to the Jahn–Teller distortion inherent in manganese ions, Mn-rich cathode materials such as $Na_4MnV(PO_4)_3$ face significant challenges in terms of electrochemical stability.[19,30] Therefore, to further optimize the amount of manganese and enhance the electrochemical properties, the introduction of an additional inexpensive active element into NVMP is a promising approach. Indeed, bimetallic doping of NVP materials is considered an effective strategy for achieving multi-electron reactions and improving both electrical conductivity and structural stability.[31] Previous research has demonstrated that the partial replacement of $Mn^{2+}$ with $Mg^{2+}$ and $Al^{3+}$ in the $Na_4MnV(PO_4)_3$ lattice significantly improves the electrochemical behavior of the host material. These modified compounds displayed smoother voltage profiles, faster $Na^+$ transport, improved rate capability, and remarkable cycling durability, retaining about 96% of their capacity after 100 cycles at 1C.[32] More recently, Xusheng Zhang and co-workers reported the successful design of $Na_{3.3}V_{1.5}Mn_{0.3}Al_{0.2}(PO_4)_3$, derived from the parent $Na_{3.5}V_{1.5}Mn_{0.5}(PO_4)_3$ through partial substitution of $Mn^{2+}$ with $Al^{3+}$. The superior performance of this new phase was attributed to the suppression of Jahn–Teller distortion, achieved by tuning the local $MnO_6$ octahedral environment and strengthening Mn–O interactions.[33]

Building upon these promising findings, a novel stoichiometry of V/Mn/Fe-based NaSICON $Na_{3.5}V_{1.5}Mn_{0.25}Fe_{0.25}(PO_4)_3$ (denoted as NVMFP) was synthesized in this work using a Pechini route. As demonstrated in our previous work,[34] the Pechini route effectively minimizes particle size, which can contribute to improving the electrochemical properties of the material. Additionally, a low-cost *ex situ* carbon coating was applied using sucrose to promote electron transfer within the NVMFP material, yielding NVMFP/C. Structural characterization confirmed the purity of the synthesized NVMFP/C powder, which crystallized in a trigonal system with the $R\bar{3}c$ symmetry. Electrochemical tests in a sodium half-cell configuration revealed that the NVMFP/C cathode delivers a discharge capacity of 167 mA h $g^{-1}$ at 0.1C over a 1.5–4.3 V potential window, corresponding to an areal capacity of ~0.30 mA h $cm^{-2}$ based on an active mass loading of ~2 mg $cm^{-2}$. This novel stoichiometry exhibits a competitive energy density compared to many reported V/Mn/Fe-based NaSICONs,[27,33,35–38] making this material a strong candidate for a high-performance SIB cathodes.

## 2. Experimental procedure

### 2.1. Material preparation

The $Na_{3.5}V_{1.5}Mn_{0.25}Fe_{0.25}(PO_4)_3$ powder was synthesized using a Pechini approach, a wet chemical method that forms a stable polymeric complex to ensure uniform distribution of the metal cations and yields ultra-fine, chemically homogeneous powders. In this synthesis, sodium nitrate ($NaNO_3$, 99.5%, Solvachim), ammonium metavanadate ($NH_4VO_3$, 99%, Sigma-Aldrich), manganese acetate ($(CH_3CO_2)_2Mn$, 98%, Sigma-Aldrich), iron oxalate dihydrate ($FeC_2O_4 \cdot 2H_2O$, 99%, Sigma-Aldrich), and ammonium dihydrogen phosphate ($NH_4H_2PO_4$, ≥99%, Sigma-Aldrich) were employed as precursors in a molar ratio of 3.5 : 1.5 : 0.25 : 0.25 : 3, respectively. Initially, $NaNO_3$, $(CH_3CO_2)_2Mn$, and $FeC_2O_4 \cdot 2H_2O$ were dissolved in 20 mL of distilled water with 4 mL of $HNO_3$ in a beaker immersed in a silicone oil bath under heating at 60 °C. $NH_4VO_3$ was then introduced, and the solution was stirred at 60 °C for 30 minutes. In parallel, citric acid (molar ratio 1 : 3 relative to metals) and $NH_4H_2PO_4$ were solubilized in 20 mL of distilled water and introduced into the mixture. A blend of ethylene glycol (99.5%, Panreac) and 10 mL of $H_2O$, with a 4 : 1 molar ratio of ethylene glycol to citric acid, was subsequently incorporated. The resulting solution was heated at 80 °C with continuous stirring until complete solvent evaporation occurred. The dried precursor was first heated in air at 190 °C for 4 hours, then ground and calcined at 750 °C for 10 hours under Ar atmosphere, using a ramp rate of 4 °C $min^{-1}$. To improve electronic conductivity, an *ex situ* carbon coating was applied. Sucrose (15 wt%) and the NVMFP powder (85 wt%) were mixed with 4 mL of acetone and ground thoroughly in an agate mortar for 20 minutes. The mixture was then pyrolyzed at 500 °C for 2 hours under an argon atmosphere with a heating rate of 5 °C $min^{-1}$ to yield the final carbon-coated product, $Na_{3.5}V_{1.5}Mn_{0.25}Fe_{0.25}(PO_4)_3$/C (NVMFP/C).

### 2.2. Material characterization

The crystal structures of NVMFP and NVMFP/C were examined using powder X-ray diffraction (XRD) on a Rigaku SmartLab diffractometer. Data were collected at ambient conditions using a 5° $min^{-1}$ scan rate, 0.02° step increments, and a $2\theta$ interval of 10–100°. Rietveld refinement was conducted using FullProf software,[39] and schematic representations of the structures were generated with Diamond software.[40] Fourier-transform infrared (FT-IR) spectra were acquired on a Bruker spectrometer, covering the mid-infrared region from 400 to 4000 $cm^{-1}$. Raman spectra were collected using a Renishaw micro-Raman spectrometer over the 500–2300 $cm^{-1}$ frequency range. Thermal stability was investigated by thermogravimetric analysis (TGA) using a NETZSCH STA analyzer in air, with temperatures ranging from 25 to 600 °C and a heating rate of 10 °C $min^{-1}$. The morphological features and elemental distribution of the powders were examined using field-emission scanning electron microscopy (FEG-ESEM-FEI) equipped with energy-dispersive X-ray spectroscopy (EDS), along with transmission electron microscopy (TEM, Talos F200S).

### 2.3. Electrochemical tests

Cathode electrodes were fabricated from a slurry containing polyvinylidene fluoride (PVDF) binder, carbon black and active material in a mass ratio of 1 : 2 : 7, using *N*-methyl-2-pyrrolidone (NMP) as solvent. The resulting slurry was applied onto the Al foil substrate and dried for 4 hours at room temperature and at 120 °C in a conventional oven for another 4 hours. After drying, the slurry was shaped into discs with a diameter of 10 mm and dried at 120 °C for 12 hours under vacuum before being transferred to an Ar-filled glove box with $H_2O$ and $O_2$ concentrations not exceeding 0.01 ppm. CR2032 coin cells were utilized to test the electrodes with an electrolyte consisting of 1 M $NaClO_4$ dissolved in a 50 : 50 (v/v) solvent mixture (ethylene carbonate (EC)/propylene carbonate (PC)) with 5 vol% of fluoroethylene carbonate (FEC). The cell configuration included sodium metal for the reference and counter electrodes and a GF/D glass fiber membrane as the separator. Electrochemical measurements, including galvanostatic cycling, cyclic voltammetry (CV), and the galvanostatic intermittent titration technique (GITT), were carried out on a Bio-Logic VMP-3 battery testing system. During the GITT experiments, the electrodes were subjected to charge/discharge steps of 30 minutes at a rate of 0.05C, each followed by a relaxation period of 2 hours. Electrochemical impedance spectroscopy (EIS) was performed by a Biologic SP-200 Potentiostat after the first charge and first discharge at C/20. The impedance data were fitted using ZView software. The electrodes had an active material mass loading of approximately 2 mg $cm^{-2}$. All electrochemical properties presented in this manuscript, including specific capacity and energy density, were normalized to the mass of the active material only. For *ex situ* XRD measurements, the cells were disassembled in an Ar-filled glove box and the electrodes were washed with dimethyl carbonate (DMC), dried, and covered with Kapton foil to prevent air exposure during data collection.

## 3. Results and discussion

### 3.1. Material characterization

NVMFP powder was successfully synthesized using a Pechini approach. The XRD patterns of NVMFP and NVMFP/C are identical (Fig. S1a). The Rietveld refinement of NVMFP/C is shown in Fig. 1a. The experimental XRD pattern displays no detectable impurities and correlates well with the calculated XRD pattern, with a satisfactory reliability factor, indicating that the structure of this phosphate is consistent with a trigonal NaSICON structure with $R\bar{3}c$ symmetry. These results also indicate the amorphous state of the coated carbon. The unit cell parameters of NVMFP/C are $a = b = 8.7892$ (2), $c = 21.7124$ (5) and $V = 1452.55$ (5) $Å^3$. Compared with those of NVP ($a = b =$ 8.72 Å, $c = 21.81$ Å, $V = 1436.46$ $Å^3$),[41] an increase in "$a$" cell parameter was observed, resulting in a larger cell volume than that of NVP. Table 1 provides the refinement details of the NVMFP/C. The unit cell of this material is illustrated in Fig. 1b, which is a three-dimensional open framework built from "lantern units" formed by edge-sharing $PO_4$ tetrahedra and $VO_6$/$MnO_6$/$FeO_6$ octahedra. Furthermore, two types of interstitial sites can host sodium atoms: Na1 site (100% occupied) with 6-fold coordination and Na2 site (80.5% occupied) with 10-fold coordination. The transition metals V, Fe and Mn share the 12c Wyckoff position with 75%, 12.5% and 12.5% occupancies, respectively. During the Rietveld refinement, the occupancies of Fe, Mn, and V sites were fixed to their nominal values after preliminary tests revealed that their simultaneous refinement caused divergence due to the strong parameter correlation, whereas individual refinement (with the other two fixed) was stable. Furthermore, this constraint improved the stability of the anisotropic displacement parameters. The elemental composition of Na, Mn and Fe was verified by Inductively Coupled Plasma (ICP) analysis (Table S1). The experimental Na/Fe and Mn/Fe ratios are in excellent agreement with those expected from the Rietveld refinement, confirming the stoichiometry of the synthesized material. The Bond Valence Sum (BVS) values (Brown & Altermatt)[42] are in agreement with the oxidation states of P1, Na1, Na2, O1 and O2, with values of 5.174 (31), 0.872 (4), 1.063 (5), 2.129 (12) and 1.985 (17) for each atom, respectively. However, for the mixed Fe1/Mn1/V1 site, the BVS values are 2.786(14), 2.989(15), and 2.854(14), yielding a total BVS of 5.7247, which exceeds 5 valence units. This indirect interpretation may indicate the presence of other species with higher oxidation state, such as $Fe^{3+}$ due to the reducing capability of the reducing agent, as observed in previous work.[43] Although the BVS analysis provides a strong indication of the electronic environment, further investigations using X-ray Photoelectron Spectroscopy (XPS) or Mössbauer remain necessary to unambiguously assign the oxidation states at the mixed V/Fe/Mn site. The details of atomic site, occupancy and BVSum obtained by Rietveld refinement are listed in Table 2. Geometric parameters are given in Table S2.

The FT-IR spectra of NVMFP and NVMFP/C materials are presented in Fig. 1c. Both samples exhibit identical band positions; however, slight differences in intensities are

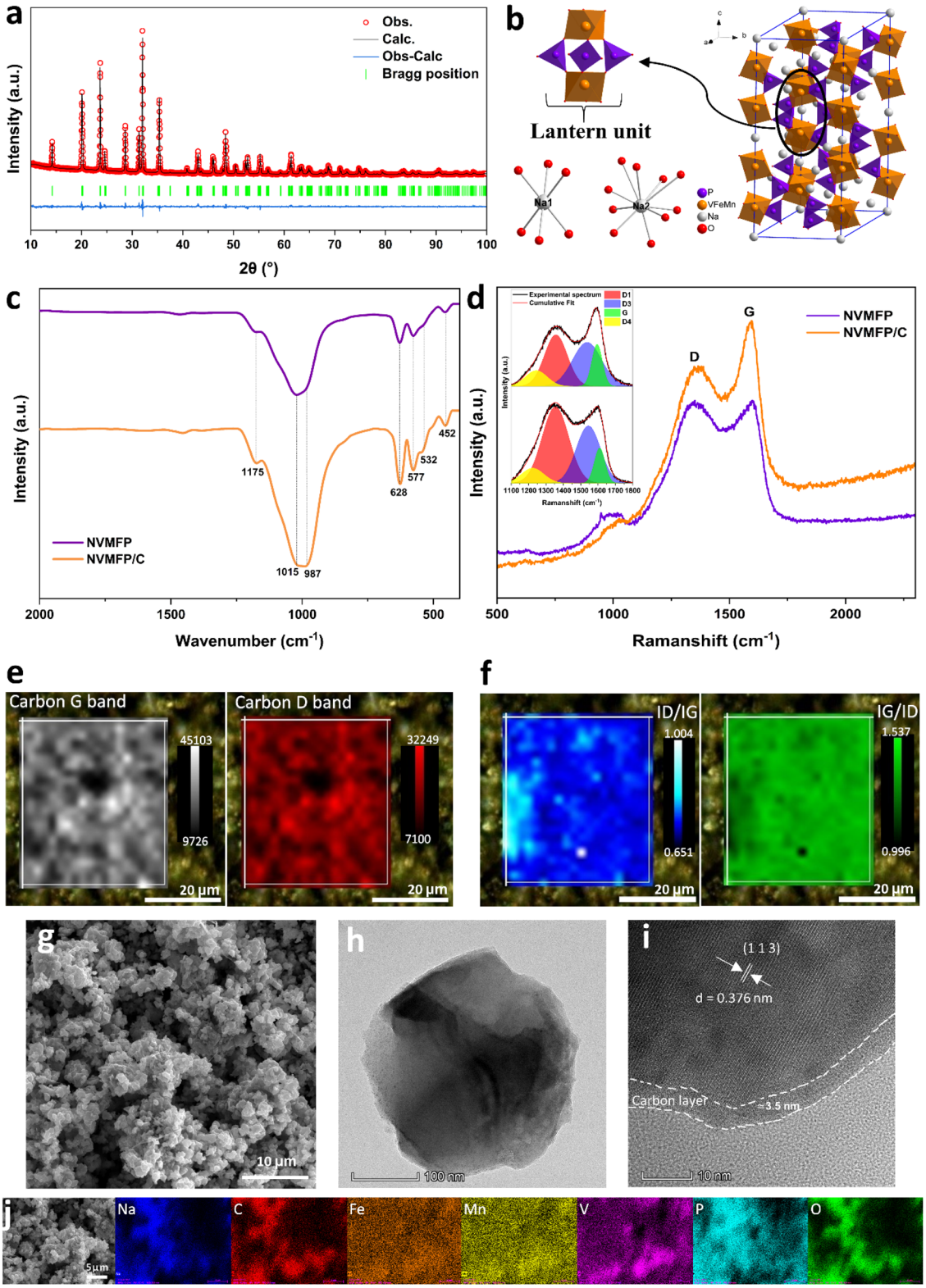


Fig. 1 (a) Rietveld refinement for the XRD pattern and (b) crystal structure visualization for NVMFP/C. (c) FT-IR and (d) Raman spectra of NVMFP and NVMFP/C. (e) Raman intensity mapping of the G and D bands, (f) $I_D/I_G$ and $I_G/I_D$ intensity ratio maps, (g) SEM, (h) TEM, (i) HR-TEM, and (j) EDS elemental mapping of NVMFP/C.

observed. The coated material exhibits high intensity, which is likely due to the improved infrared absorption conferred by the carbon layer.[44] The detected absorption bands correspond entirely to the vibration modes of the $[PO_4]^{3-}$ ion: $\nu_3$ (P–O) around 1175 $cm^{-1}$ and 1015 $cm^{-1}$; $\nu_1$ (P–O) around 987 $cm^{-1}$; $\nu_4$ (P–O) around 628 $cm^{-1}$, 577 $cm^{-1}$, and 532 $cm^{-1}$, and $\nu_2$ (P–O)

Table 1 Crystallographic data, data acquisition and structural refinement for NVMFP/C

| | |
|---|---|
| **Crystallographic data** | |
| Chemical formula | $Na_{3.5}V_{1.5}Mn_{0.25}F_{0.25}(PO_4)_3$ |
| $M_r$ (g mol$^{-1}$) | 469.4887 |
| Crystal symmetry | Trigonal, $R\bar{3}c$ |
| X-ray source | Cu Ka ($\lambda$ = 1.5406 Å) |
| Temperature (K) | 298 |
| $a$, $c$ (Å) | 8.78915 (14), 21.7124 (5) |
| $V$ (Å$^3$) | 1452.55 (5) |
| $Z$ | 6 |
| **Data acquisition** | |
| Diffractometer | Rigaku SmartLab |
| $2\theta$ values (°) | $2\theta_{min} = 10$, $2\theta_{max} = 100$, $2\theta_{step} = 0.02$ |
| **Refinement** | |
| Reliability factors | $R_p = 4.387$, $R_{wp} = 5.517$, $R_{exp} = 4.385$, $R_{Bragg} = 3.856$, $\chi^2 = 1.58$ |
| Refined parameters | 94 |
| Collected data points | 4500 |

located at 452 cm$^{-1}$. These findings are in agreement with those reported in earlier studies.[34,45] Fig. 1d displays the Raman spectra of NVMFP and NVMFP/C, showing the presence of two peaks at 1350 cm$^{-1}$ (D-band) and 1590 cm$^{-1}$ (G-band), attributable to carbon, as well as an additional band at 1000 cm$^{-1}$ corresponding to the $PO_4$ stretching vibrations. The weak G and D bands observed in the NVMFP sample confirm the presence of minor residual carbon originating from the decomposition of citric acid and ethylene glycol during the calcination step. In contrast, the increased intensity of the carbon bands accompanied by the attenuation of the $PO_4$ band in NVMFP/C provides direct evidence of the higher carbon content in the composite.[46] To accurately quantify the structural evolution of the carbon coating, a Raman deconvolution of the D and G bands (inset in Fig. 1d and Table S3) was performed according to previous work.[47] The $I_{D_4}/I_G$ ratios ($D_4$ peak intensity/G peak intensity) for NVMFP and NVMFP/C samples are comparable. However, the $I_{D_3}/I_G$ ratio is higher for NVMFP than for NVMFP/C, while the $I_{D_1}/I_G$ ratio is approximately twice as high for NVMFP. Additionally, NVMFP/C exhibits the lowest Full Width at Half Maximum (FWHM) values for both the $D_1$ and G bands, with values of 77.6917 and 36.1320, respectively (resulting in $D_{1(FWHM)}/G_{(FWHM)}$ ratio of 2.1502). These Raman results suggest that NVMFP/C possesses a more ordered carbon structure than NVMFP, as evidenced by its lower $I_{D_1}/I_G$ and $I_{D_3}/I_G$ ratios and narrower $D_1$ and G Raman bands, indicative of larger graphitic domains. It has been reported that the increase in the graphitic character of carbon, reflected by an increased $sp^2$ carbon content, is responsible for improved electrical conductivity through the formation of extended graphitic π-electron networks.[48–50] Raman mapping, shown in Fig. 1e and f, was employed to investigate the carbon distribution on the NVMFP/C grain surfaces by comparing the spatial intensities of the D and G bands, alongside both $I_D/I_G$ and $I_G/I_D$ intensity ratio maps. The overlapping and homogeneous distribution of G and D signals (Fig. 1e) confirms a uniform carbonaceous coating on the grain surfaces of NVMFP/C. The intensity ratio maps (Fig. 1f) reveal a predominance of graphitic character, although a small area exhibiting characteristic D-band features is observed, indicating localized structural disorder. The average carbon cluster size $L_a$ of NVMFP/C calculated using the Tuinstra–Koenig method (Note S1) is 4.09 nm. The TGA measurements (Fig. S1b) revealed carbon contents of about 2 wt% and 2.87 wt% for NVMFP and NVMFP/C, respectively. The microstructure of NVMFP/C powder was investigated by electron microscopy (SEM and TEM). As displayed in Fig. 1g and h, the NVMFP/C particles have sizes ranging from 0.3 to 1 μm with irregular shapes. Lattice fringes with a spacing of 0.376 nm are visible in the HR-TEM image (Fig. 1i), which is consistent with the $d_{hkl}$ value for the (113) plane of the NVMFP/C, indicating

Table 2 Atomic coordinates, displacement parameters (Å$^2$), site occupancy rate and BVS calculation for NVMFP/C

| Atom | Wyckoff position | $x$ | $y$ | $z$ | Uiso | Occ. (<1) | BVSum |
|---|---|---|---|---|---|---|---|
| Na1 | 6b | 0.00000 | 0.00000 | 0.00000 | 0.116 (5) | | 0.872 (4) |
| Na2 | 18e | 0.6364 (6) | 0.00000 | 0.25000 | 0.049 (3) | 0.805 (7) | 1.063 (5) |
| Fe1 | 12c | 0.00000 | 0.00000 | 0.14767 (9) | 0.0154 (8) | 0.12501 | 2.786 (14) |
| Mn1 | 12c | 0.00000 | 0.00000 | 0.14767 (9) | 0.0154 (8) | 0.12501 | 2.989 (15) |
| V1 | 12c | 0.00000 | 0.00000 | 0.14767 (9) | 0.0154 (8) | 0.75000 | 2.854 (14) |
| P1 | 18e | 0.2921 (3) | 0.00000 | 0.25000 | 0.0159 (10) | | 5.174 (31) |
| O1 | 36f | 0.1919 (4) | 0.1686 (5) | 0.0897 (2) | 0.0134 (13) | | 2.129 (12) |
| O2 | 36f | 0.0259 (6) | 0.2106 (5) | 0.19288 (16) | 0.0266 (17) | | 1.985 (17) |

that the particles possess a high degree of crystallinity. In addition, the presence of an amorphous carbon shell approximately 3.5 nm thick was observed on the surface of the crystallized particles, which is in excellent agreement with the value calculated from the Raman spectra (~4 nm). EDS mapping (Fig. 1j) indicates a uniform distribution of Na, V, Fe, Mn, O, C, and P throughout the NVMFP/C particles.

### 3.2. Electrochemistry

The electrochemical investigation of NVMFP/C and NVMFP cathode materials within the voltage window of 1.5–4.3 V *vs.* $Na^+/Na$ was examined using CR2032 coin cells (1C ~ 114.2 mA $g^{-1}$ which is defined as 2 $Na^+$ exchange in 1 hour). Electrochemical comparisons between NVMFP/C and NVMFP cathodes (Fig. S2) were performed based on the second galvanostatic cycle to ensure a complete evaluation of the redox transitions across the full potential range (1.5–4.3 V). This approach accounts for the capacity contributions below the open-circuit voltage, which are not fully captured during the initial charging process. A notable difference in specific charge capacity at 0.1C was observed between the two cathodes, with NVMFP/C exhibiting a higher charge capacity of approximately 167 mA h $g^{-1}$ (~0.30 mA h $cm^{-2}$) compared to 130 mA h $g^{-1}$ (~0.23 mA h $cm^{-2}$) for NVMFP. The enhanced capacity observed between the pristine and carbon-coated Fe-modified phase, notwithstanding a slight increment in the amount of carbon (from ~2.0 wt% to ~2.87 wt%), is due to the improved electronic conductivity achieved by the *ex situ* carbon coating, which promotes charge transfer within NVMFP cathode material, as evidenced by the Raman results. Fig. 2a demonstrates the first three charge/discharge cycles of NVMFP/C cathode at 0.1C. The electrode delivers initial charge and discharge capacities of 141 mA h $g^{-1}$ (~0.25 mA h $cm^{-2}$) and 167 mA h $g^{-1}$ (~0.30 mA h $cm^{-2}$), respectively. Two distinct charge/discharge voltage plateaus are observed at approximately 3.42 V and 4.0 V, matching well with the $V^{4+}/V^{3+}$, $Mn^{3+}/Mn^{2+}$ and $V^{5+}/V^{4+}$ redox couples, respectively.[33,51,52] An additional, smaller plateau appears near 2.62 V, consistent with the potential range of the $Fe^{3+}/Fe^{2+}$ redox activity in the NaSICON framework.[18,37,53] Moreover, a pseudo-plateau around 3.15 V is evident during charge, which may result from the extraction of $Na^+$ from two distinct crystallographic sites within the NVMFP/C framework, a phenomenon previously reported in related studies.[25,27] In the second cycle, a new charge/discharge plateau emerges at around 1.7 V, aligning with the expected potential for the $V^{3+}/V^{2+}$ redox couple,[51,52] which provides an additional 20 mA h $g^{-1}$ to the charge capacity. Consequently, the total charge and discharge capacities are 167 mA h $g^{-1}$ (~0.30 mA h $cm^{-2}$) (extraction of approximately 2.94 $Na^+$ ions per formula unit) and 164 mA h $g^{-1}$ (~0.29 mA h $cm^{-2}$), respectively, achieving a coulombic efficiency of 98.23% in the second cycle. The d$Q$/d$V$ plot (Fig. 2b) derived from the second cycle of NVMFP/C cathode further corroborates the aforementioned cycling results by providing a clear signature of the redox transitions. Specifically, a pair of peaks at high potential is clearly evidenced, in good agreement with the $V^{5+}/V^{4+}$ transition. Additionally, shouldered and intense oxidation/reduction peaks were observed, which could correspond to the overlapping $V^{4+}/V^{3+}$ and $Mn^{3+}/Mn^{2+}$ couples, likely due to their similar redox potentials in the NaSICON framework. In contrast, a faint signal (inset in Fig. 2b), barely discernible from the baseline, could be attributed to the $Fe^{3+}/Fe^{2+}$ redox feature. Notably, peak splitting is observed at approximately 1.7 V during reduction and at 3.14 V during oxidation; these features can be attributed to the multi-step electrochemical insertion and extraction of $Na^+$ into the NaSICON structure, as observed in related studies.[25,54] Remarkably, NVMFP/C electrode requires a presodiation treatment to achieve its full capacity. It is worth noting that the NVMFP/C electrode shows a capacity discrepancy of 26 mA h $g^{-1}$ between the first charge and discharge cycles, corresponding to approximately 0.45 moles of $Na^+$. This surplus suggests a resodiation mechanism, where additional sodium ions are incorporated into the lattice to occupy the limited interstitial space of 4 $Na^+$ available within the NaSICON framework,[54] which can lead to $Na_4V_{1.5}Mn_{0.25}Fe_{0.25}(PO_4)_3$ phase at a lower voltage ~1.6 V. Consequently, the first-cycle irreversibility can be attributed primarily to Na inventory increase, where additional $Na^+$ are inserted into the framework. Furthermore, the presodiation process can be mitigated through material optimization, notably by developing sodium-rich cathodes. However, this approach remains complex due to the need for precise stoichiometric control and demanding synthesis conditions. Alternatively, electrolyte optimization offers a strategy to regulate this phenomenon, particularly in full-cell configurations, through the incorporation of sacrificial sodium-source additives.[55,56] The cyclic voltammograms of the NVMFP/C electrode at 0.8 mV $s^{-1}$ (Fig. 2c) display four distinct redox peak pairs at 1.82/1.5 V, 3.33/2.99 V, 3.70/3.26 V, and 4.06/3.89 V attributed to the $V^{3+}/V^{2+}$, the split $Na^+$ extraction phenomenon, the $V^{4+}/V^{3+}$($Mn^{3+}/Mn^{2+}$) couples and the $V^{5+}/V^{4+}$ couple, respectively. However, the $Fe^{2+}/Fe^{3+}$ redox peaks are not clearly distinguishable in the CV curves, despite their contribution being evidenced by a smaller plateau in the galvanostatic test. A similar behavior was reported in a previous study.[43] The cycling stability of both high- and low-voltage regions was investigated over 50 cycles at 0.5C (Fig. S3). It is observed that both high- and low-voltage contributions remain significant throughout the cycling. However, a noticeable capacity fade was recorded, with a capacity retention of only 75%, which may be attributed to electrolyte decomposition resulting from prolonged exposure to both potential extremes. It is reported in the literature that, at high voltage, the Cathode Electrolyte Interphase (CEI) suffers from poor self-healing capability and dissolution, which negatively affects cycle life.[57,58] Notably, the coulombic efficiency of NVMFP/C at 0.5C remained stable and higher than 95% over 50 cycles, indicating that while some capacity is lost, the remaining redox processes maintain high reversibility and the parasitic reactions are relatively limited. These findings confirm the successful activation of multiple redox centers and their cyclability, highlighting the benefits of this specific stoichiometry.

The rate performance of the NVMFP/C electrode is shown in Fig. 2d. The NVMFP/C cathode provides initial discharge capacities of 146, 134, 119, 101, and 97 mA h $g^{-1}$, corresponding

 

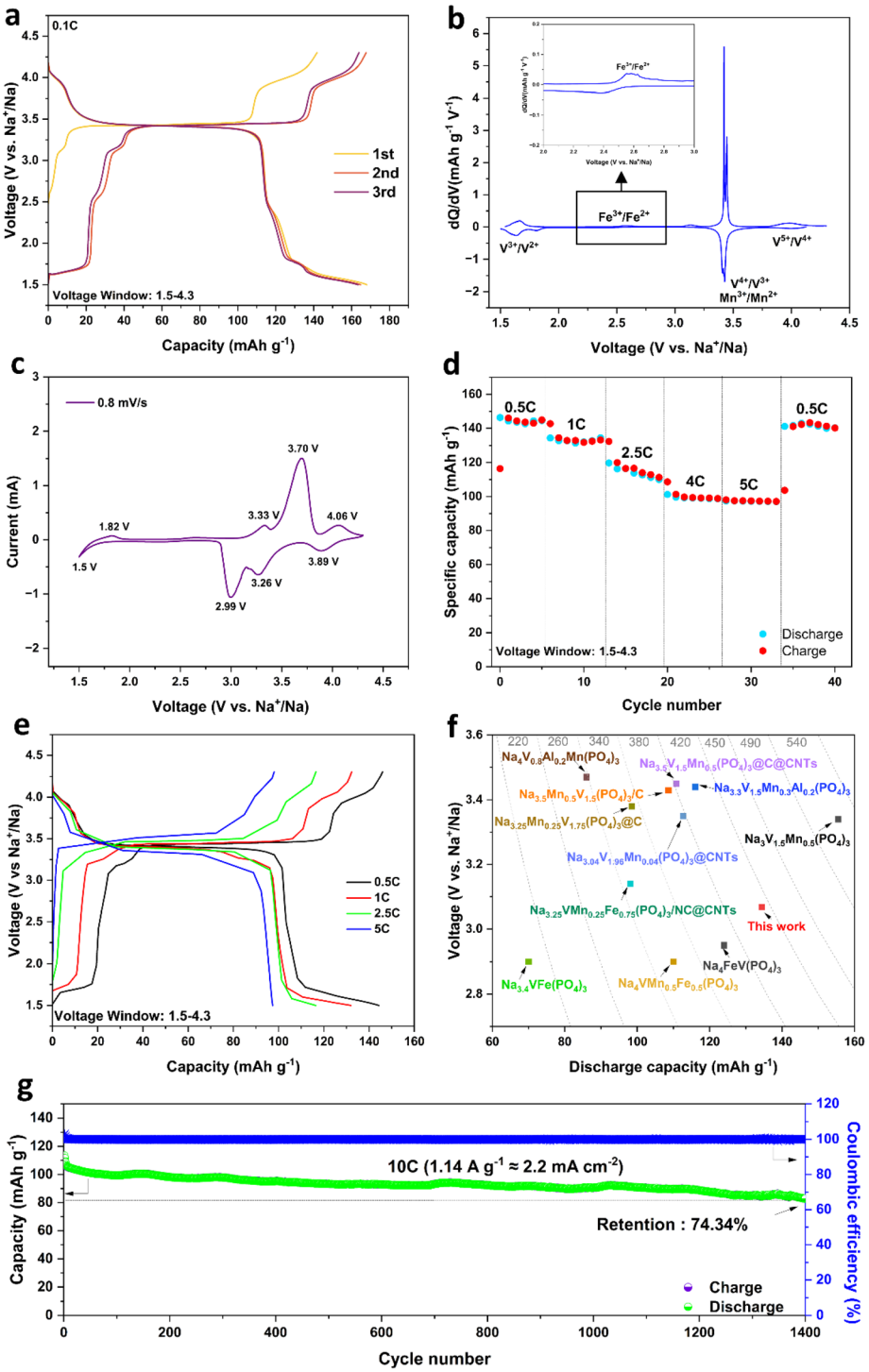


Fig. 2 (a) Charge–discharge profile of NVMFP/C cathode at 0.1C, (b) d$Q$/d$V$ curve of the second cycle for NVMFP/C at C/20, (c) CV curve of NVMFP/C electrode in the voltage window of 1.5–4.3 V at a scan rate of 0.8 mV $s^{-1}$, (d) rate capability of NVMFP/C cathode and (e) corresponding second-cycle charge–discharge curves, (f) the average voltage and first discharge capacity of NVMFP/C cathode, compared with other reported V-based NaSICON cathodes (at 1C) (for reference see Table S4), (g) cycle life of NVMFP/C cathode at 10C in the voltage range of 1.5–4.3 V.

approximately to 0.27, 0.25, 0.22, 0.19 and 0.18 mA h $cm^{-2}$ at 0.5, 1, 2.5, 4 and 5C current rates, respectively. When the current rate was returned to 0.5C, the NVMFP/C electrode recovered a specific discharge capacity of 141 mA h $g^{-1}$ (~0.26 mA h $cm^{-2}$), indicating its remarkable reversibility and structural stability. The charge/discharge profiles with the increased rate as shown in Fig. 2e. It is clearly observed that the contribution of both high- and low-potential regions to the total capacity decreases as the C-rate increases. At 5C, the capacity is primarily sustained by the $V^{4+}/V^{3+}$ and $Mn^{3+}/Mn^{2+}$ redox

regions. Interestingly, the NVMFP/C cathode exhibited an excellent energy density of 412 Wh $kg^{-1}$ at 1C, and is well-positioned among the highest values reported for V/Mn/Fe-based NaSICON systems (Fig. 2f and Table S4). The long-term cycling performance of the NVMFP/C cathode was evaluated at a high rate of 10C (Fig. 2g). The electrode delivered an initial specific capacity of 111 mA h $g^{-1}$ (~0.22 mA h $cm^{-2}$) and retained 82 mA h $g^{-1}$ (~0.16 mA h $cm^{-2}$) after 1400 cycles, corresponding to capacity retention of 74.34%. This excellent cycling stability highlights the robust structural integrity of the material, which enables highly reversible sodiation/desodiation within the wide voltage range of 1.5–4.3 V. To further evaluate the kinetic stability of the cell at 10C, the polarization during long-term cycling was analyzed (Fig. S4). The polarization decreases from 0.39 V at cycle 1 to 0.22 V at cycle 10, then gradually increases to 0.47 V at cycle 100, 0.74 V at cycle 1000, and reaches 1 V at cycle 1400. The initial decrease may be related to a stabilization or activation process during the early cycles. While the present results do not allow a definitive identification of the underlying mechanisms, the observed polarization growth could suggest cumulative interfacial occurring during prolonged cycling. Overall, the charge/discharge profiles exhibit minimal evolution during cycling that indicates well-preserved electrochemical kinetics. This is further supported by *ex situ* XRD (Fig. S6b) analysis after cycling, which confirms that the characteristic peaks of the NaSICON framework remain intact. The absence of structural degradation or secondary phase formation demonstrates the robust structural integrity of the NVMFP/C cathode during long-term cycling. Furthermore, *ex situ* XRD diagrams of the NVMFP/C electrode at different voltage stages during the first cycle at C/10 (Fig. S6a) demonstrate that the NaSICON structure undergoes reversible structural evolution, which confirms its structural stability during sodium insertion/extraction processes.

### 3.3. Charge storage behavior and Na-ion kinetics

The charge storage behavior and $Na^+$ ion transport kinetics of NVMFP/C were evaluated using cyclic voltammetry (CV) at various sweep rates and the galvanostatic intermittent titration technique (GITT). From the cyclic voltammograms (Fig. 3a), the $Na^+$ diffusion coefficient ($D_{Na^+}$) and the charge storage behavior were analyzed by employing the following equations:

$$i_p = 2.69 \times 10^5 n^{3/2} S D_{Na}{}^{1/2} C_0 \nu^{1/2} \text{ (Randles–Sevcik equation)} \quad (1)$$

$$i_p = a\nu^b \quad (2)$$

$$i = k_1\nu + k_2\nu^{1/2} \quad (3)$$

where $i_p$ is the peak current (A), $n$ is the number of electrons transferred, and S is the electrode surface area (0.79 $cm^2$), $D_{Na^+}$ is the diffusion coefficient ($cm^2$ $s^{-1}$), $C_{Na}$ is the molar concentration of Na ion ($2.39 \times 10^{-2}$ mol $cm^{-3}$), $\nu$ is the scan rate (V $s^{-1}$), $a$, $b$, $k_1$, and $k_2$ are adjustable parameters that are determined by the fitting results between $i_p$ and $\nu$.

The diffusion coefficients $D_{Na^+}$ were estimated using the Randles–Sevcik equation, assuming a reversible, diffusion-controlled electrochemical process based on the linear relationship between the peak currents (O1, O2, O3, R1, R2 and R3) and the square root of the scan rate ($\nu^{1/2}$) as presented in Fig. 3b. The peak currents (O1, O2, O3, R1, R2 and R3) were determined at the maximum intensity of each identified redox process, as the well-defined nature of the peaks allowed for a consistent selection across all scan rates. The slope obtained from the linear fit, combined with eqn (1), yielded $D_{Na^+}$ values (Table 3) ranging from $1.87 \times 10^{-11}$ to $5.38 \times 10^{-12}$ $cm^2$ $s^{-1}$, which is comparable to those of typical cathode materials with a NaSICON structure.[25,37] It is important to emphasize that the Randles–Sevcik equation used in these calculations only describes faradaic-controlled processes while neglecting any pseudocapacitive contributions. Nevertheless, the $Na^+$ insertion/extraction mechanism can be rationalized by analyzing the $b$-value obtained from eqn (2). Depending on the value of $b$, two distinct charge storage behaviors can be distinguished: (i) a diffusion-controlled process when $b \sim 0.5$, corresponding to semi-infinite ion diffusion in the solid-state host lattice, and (ii) a capacitive-controlled process when $b \sim 1.0$, associated with surface or pseudocapacitive contributions. As shown in Fig. 3c and Table S5, the linear fit of $\log(i_p)$ *versus* $\log(\nu)$ yields a slope ($b$) ranging from 0.49 to 1, which suggests a mixture of faradaic intercalation and pseudocapacitive mechanisms.[58] The contribution of each mechanism to the $Na^+$ insertion/de-insertion in NVMFP/C electrode was evaluated using eqn (3). This equation contains two types of current: capacitive current ($k_1\nu$) and diffusion-limited current ($k_2\nu^{1/2}$). Fig. 3d displays the capacitive and the diffusion contributions *versus* scan rate ($\nu$). At a scan rate of 0.8 mV $s^{-1}$, the capacitive process accounted for 63% of the total current (Fig. 3e). With increasing scan rate from 0.8 to 2 mV $s^{-1}$, the capacitive contribution increases from 63% to 73%. This clearly shows that capacitive behavior dominates the electrochemical reaction process of NVMFP/C cathode. Due to the minimal carbon content of our material, the capacitive dominant processes can be attributed to the small particle sizes and optimized interface, achieved by the Pechini approach, which facilitates surface-controlled reaction kinetics.[59,60]

The apparent diffusion coefficient of $Na^+$ ($D_{Na^+}$) was also calculated from GITT measurements using eqn (4). This method is considered more precise because it operates under near-equilibrium conditions, providing a more reliable measurement of the $Na^{1+}$ diffusion coefficients.

$$D_{Na^+} = \frac{4}{\pi}\left(\frac{IV_M}{nFS}\right)^2 \left[\left(\frac{dV}{dx}\right) \Big/ \left(\frac{dV}{d\sqrt{t}}\right)\right]^2 \left(t \ll \frac{L^2}{D}\right) \quad (4)$$

The parameter $I$ corresponds to the applied current, while $V_M$ denotes the molar volume of the electrode material ($cm^3$ $mol^{-1}$). The symbol $n$ designates the number of electrons involved in the charge-transfer process, and $F$ refers to Faraday's constant (A s $mol^{-1}$). The term $S$ represents the electrode surface area (0.79 $cm^2$). The derivative $dV/dx$ expresses the slope of the potential variation as a function of sodium composition

 

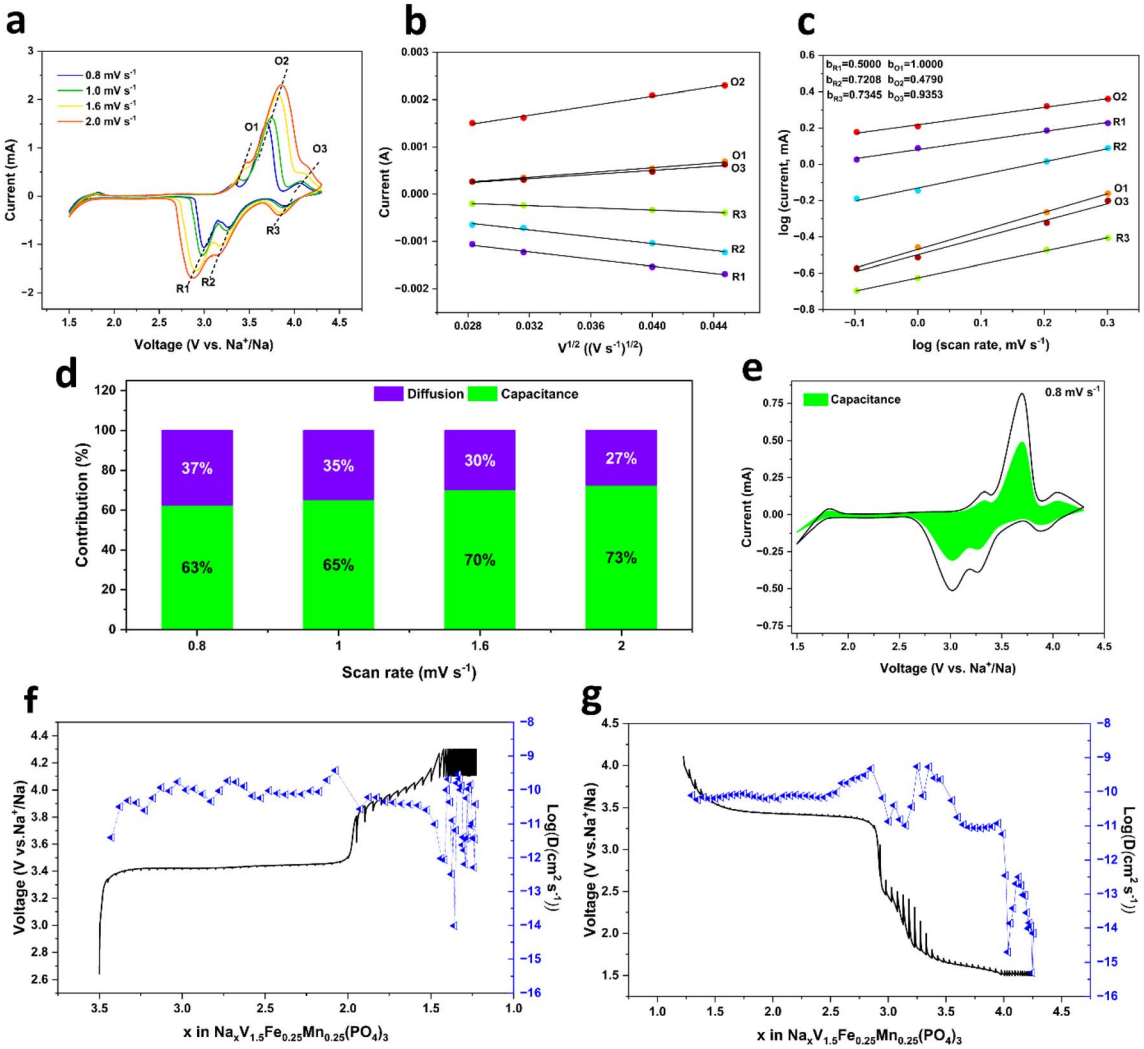


Fig. 3 (a) CV curves of NVMFP/C electrode at various scan rates, (b) the current as a function of the square root of the scan rates, (c) log (current) *versus* log (scan rate), (d) pseudocapacitive contribution at various scan rates, (e) the capacitive contribution to the total current at 0.8 mV $s^{-1}$, and (f) and (g) the GITT curves for (f) charge and (g) discharge as a function of the $Na^+$ concentration in $Na_xV_{1.5}Mn_{0.25}Fe_{0.25}(PO_4)_3$.

(V $mol^{-1}$), whereas $dV/d\sqrt{t}$ corresponds to the slope of the potential *versus* $\sqrt{t}$ curve, obtained from the voltage–time profile (V $s^{-1/2}$). Fig. 3f and g show the charge/discharge GITT curves and the variation of the apparent diffusion coefficient as a function of $Na^+$ concentration in $Na_xV_{1.5}Fe_{0.25}Mn_{0.25}(PO_4)_3$. During the charge/discharge process, the voltage plateau around 3.5 V exhibits a smaller overpotential, corresponding to an apparent diffusion coefficient of approximately $10^{-11}$ $cm^2$ $s^{-1}$. However, when the voltage is either higher or lower than 3.5 V, the overpotential increases, and the apparent diffusion coefficient fluctuates between different values. At low voltages during discharge, a significant drop in the apparent diffusion coefficient was observed due to high occupation of vacancy sites by $Na^+$ sodiation, which hinders further sodium insertion within the material's structure.[13]

EIS measurements were conducted on the NVMFP/C electrode after first charge and first discharge (Fig. 4). The inset in Fig. 4 displays the equivalent circuit used to fit this response, which consists of several components: a resistance ($R_O$) at a higher frequency, representing the ohmic resistance due to the electrolyte; a resistance ($R_{CEI}$) in parallel with a constant phase element ($CPE_{CEI}$) at intermediate frequency, describing the Cathode-Electrolyte Interphase (CEI) layer response; a resistance ($R_{ct}$) connected in series with a Warburg element (W), both of which are in parallel with a constant phase element ($CPE_{ct}$) at lower frequency. This last combination corresponds

Table 3 Diffusion coefficient of redox peaks for the NVMFP/C cathode

| Peak | R1 | R2 | R3 | O1 | O2 | O3 |
|---|---|---|---|---|---|---|
| $D_{Na^+}$ ($cm^2$ $s^{-1}$) | $5.58 \times 10^{-11}$ | $5.17 \times 10^{-11}$ | $5.38 \times 10^{-12}$ | $2.52 \times 10^{-11}$ | $9.78 \times 10^{-11}$ | $1.87 \times 10^{-11}$ |

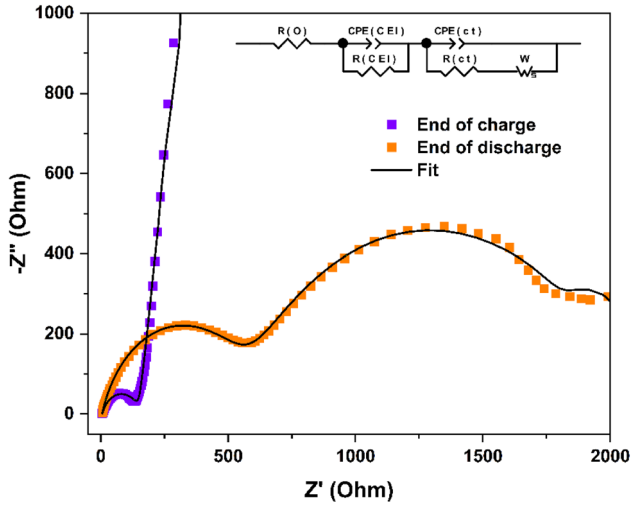


Fig. 4 EIS spectra of NVMFP/C electrode after first charge/discharge at C/20.

to faradaic impedance, where $R_{ct}$/$CPE_{ct}$ is indicative of the charge transfer process, and the Warburg impedance (W) represents the diffusion of $Na^+$ at the electrode–electrolyte interfaces. Table S8 summarizes the fitting parameters of NVMFP/C after first charge and first discharge. At the end of the first charge, the EIS plot shows a single semi-circle, which corresponds to the CEI layer response, followed by a diffusion line.[61] At this stage, the $R_{CEI}$ and $R_{ct}$ resistance values are 143.4 and 2090 Ω, respectively. The higher $R_{ct}$ prevents the formation of a distinct charge-transfer semi-circle. After the first discharge, the $R_{CEI}$ and $R_{ct}$ resistance show values of 550.2 and 1462 Ω, respectively, and an additional semi-circle appears. This new semi-circle corresponds to the charge transfer response and can indicate the domination of electrochemical intercalation reaction at this stage. This behavior was observed in previous work dealing with Li-ion system, in which a dominant intercalation–deintercalation process occurs.[62] Moreover, the significant increase in $R_{CEI}$ after the first discharge is a consequence of the CEI growth caused by the decomposition of the electrolyte.[63] Furthermore, $R_{ct}$ remained relatively high at the end of both charge and discharge, indicating persistent interfacial limitations. The high value of $R_{ct}$ may result from several combined factors, including the electrode thickness, which increases ionic transport pathways, and the electrolyte composition. Although $NaClO_4$ in EC : PC with FEC provides good bulk conductivity, FEC decomposition and high-voltage operation (4.3 V) can promote the formation of a resistive CEI layer, thereby increasing interfacial impedance.[64] Despite the relatively high $Na^+$ diffusion observed by GITT within the NaSICON-type NVMFP/C framework, $R_{ct}$ is mainly governed by interfacial charge-transfer processes, explaining why it remains in the kiloohm range.

## 4. Conclusion

In summary, we report the successful design and synthesis of $Na_{3.5}V_{1.5}Mn_{0.25}Fe_{0.25}(PO_4)_3$ (NVMFP/C), a novel V/Mn/Fe-based NaSICON-type cathode material, *via* the Pechini method followed by an *ex situ* carbon coating. Structural and morphological characterizations using XRD, FT-IR, Raman, TGA, SEM, EDS, and TEM confirm the formation of a highly crystalline, phase-pure trigonal NaSICON framework with uniform particle distribution and homogeneous elemental composition. The electrochemical evaluation of NVMFP/C as a cathode material for SIBs demonstrates a high reversible capacity of 167 mA h $g^{-1}$ (~0.30 mA h $cm^{-2}$) within a wide voltage window of 1.5–4.3 V at 0.1C, enabled by the activation of multi-electron redox reactions. The material achieves a remarkable energy density of 412 Wh $kg^{-1}$ at 1C, good rate capability, and remarkable long-term cycling stability, retaining 74% of its initial capacity after 1400 cycles at 10C. These outstanding performances are attributed to a combination of rapid $Na^+$ diffusion through the robust 3D framework, enhanced electronic conductivity and structural integrity during repeated sodiation/desodiation achieved by the synergy between Fe-incorporation, Pechini-derived nanostructure, and the low-cost *ex situ* carbon coating. Kinetic studies using cyclic voltammetry, GITT, and EIS reveal a significant capacitive contribution, indicating that surface-controlled processes play a key role in facilitating fast charge storage. The synergy between bulk diffusion and pseudocapacitive kinetics underpins the superior rate performance and high-energy output of NVMFP/C. This work highlights that careful compositional engineering, multi-electron redox activation, and microstructural optimization can be strategically combined to develop NaSICON-type cathodes with high energy density, rapid kinetics, and long-term durability.

## Author contributions

Loubna Chayal: data curation, formal analysis, investigation, methodology, writing – original draft, Soraia El Moutchou: data curation, software, Noha Sabi: data curation, formal analysis, Hicham Ben Youcef: project administration, resources, Hasna Aziam: supervision, validation, writing – review & editing, Mohamed Saadi: supervision, validation, project administration, resources, and Mohammed Hadouchi: supervision, methodology, validation, writing – review & editing, project administration, resources.

## Conflicts of interest

There are no conflicts of interest to declare.

## Data availability

Data are available in the supplementary information (SI) or from the corresponding author upon reasonable request. Supplementary information: notes S1, S2 and S3, Fig. S1, S2, S3, S4, S5 and S6, and Tables S1, S2, S3, S4, S5, S6, S7 and S8. See DOI: https://doi.org/10.1039/d6ra00418k.

## Acknowledgements

Financial support from the CNRST was provided through the "PhD-Associate Scholarship – PASS" Program (74 UM5R2023). The authors sincerely thank UATRS-CNRST for facilitating access to the transmission electron microscope. Loubna Chayal also acknowledges UM6P for financial support during her research stay at HTMR-UM6P.

## References

1 Y. Lu, Q. Zhang and J. Chen, Recent progress on lithium-ion batteries with high electrochemical performance, *Sci. China:Chem.*, 2019, **62**, 533–548, DOI: 10.1007/s11426-018-9410-0.

2 V. M. Leal, J. S. Ribeiro, E. L. D. Coelho and M. B. J. G. Freitas, Recycling of spent lithium-ion batteries as a sustainable solution to obtain raw materials for different applications, *J. Energy Chem.*, 2023, **79**, 118–134, DOI: 10.1016/j.jechem.2022.08.005.

3 C. Vaalma, D. Buchholz, M. Weil and S. Passerini, A cost and resource analysis of sodium-ion batteries Christoph, *Nat. Rev. Mater.*, 2018, **3**, 18013, DOI: 10.1038/natrevmats.2018.13.

4 S. Srinivasan, S. Shanthakumar and B. Ashok, Sustainable lithium-ion battery recycling: a review on technologies, regulatory approaches and future trends, *Energy Rep.*, 2025, **13**, 789–812, DOI: 10.1016/j.egyr.2024.12.043.

5 T. Jin, H. Li, K. Zhu, P. F. Wang, P. Liu and L. Jiao, Polyanion-type cathode materials for sodium-ion batteries, *Chem. Soc. Rev.*, 2020, **49**, 2342–2377, DOI: 10.1039/c9cs00846b.

6 P. K. Nayak, L. Yang, W. Brehm and P. Adelhelm, From Lithium-Ion to Sodium-Ion Batteries: Advantages, Challenges, and Surprises, *Angew. Chem., Int. Ed.*, 2018, **57**, 102–120, DOI: 10.1002/anie.201703772.

7 Q. Zheng, H. Yi, X. Li and H. Zhang, Progress and prospect for NASICON-type $Na_3V_2(PO_4)_3$ for electrochemical energy storage, *J. Energy Chem.*, 2018, **27**, 1597–1617, DOI: 10.1016/j.jechem.2018.05.001.

8 Y. Fang, L. Xiao, Z. Chen, X. Ai, Y. Cao and H. Yang, Recent Advances in Sodium-Ion Battery Materials, *Electrochem. Energy Rev.*, 2018, **1**, 294–323, DOI: 10.1007/s41918-018-0008-x.

9 D. Fan, Y. Wang, X. Zhao, J. Jin, Q. Shen, Z. Li, X. Qu, L. Jiao, Y. Liu and Z. Guo, A novel NASICON-$Na_{3.4}MnV_{0.2}Cr_{0.2}Ti_{0.6}(PO_4)_3$ cathode with ultrahigh energy density and remarkable cycling stability toward practical Na-ion batteries, *Mater. Today*, 2025, **86**, 63–73, DOI: 10.1016/j.mattod.2025.03.010.

10 W. Li, J. Li, R. Li, X. Li, J. Gao, S. M. Hao and W. Zhou, Study on sodium storage properties of manganese-doped sodium vanadium phosphate cathode materials, batter, *Energy*, 2023, **2**, 1–11, DOI: 10.1002/bte2.20220042.

11 Z. Lv, M. Ling, M. Yue, X. Li, M. Song, Q. Zheng and H. Zhang, Vanadium-based polyanionic compounds as cathode materials for sodium-ion batteries: toward high-energy and high-power applications, *J. Energy Chem.*, 2021, **55**, 361–390, DOI: 10.1016/j.jechem.2020.07.008.

12 Q. Cheng, X. Zhao, G. Yang, L. Mao, F. Liao, L. Chen, P. He, D. Pan and S. Chen, Recent advances of metal phosphates-based electrodes for high-performance metal ion batteries, *Energy Storage Mater.*, 2021, **41**, 842–882, DOI: 10.1016/j.ensm.2021.07.017.

13 J. Hou, T. Chen, M. Ait Tamerd, J. Liu, W. H. Huang, M. Hadouchi, Y. Zhu, X. Shi, S. Guo, M. Yang, Y. Shi, M. Tang and J. Ma, Activating fast and reversible sodium storage in NASICON cationic defect sites through fluorine doping, *Nat. Commun.*, 2025, **16**, 1–11, DOI: 10.1038/s41467-025-58012-0.

14 R. Thirupathi, V. Kumari, S. Chakrabarty and S. Omar, Recent progress and prospects of NASICON framework electrodes for Na-ion batteries, *Prog. Mater. Sci.*, 2023, **137**, 101128, DOI: 10.1016/j.pmatsci.2023.101128.

15 Z. Jian, Y. S. Hu, X. Ji and W. Chen, NASICON-Structured Materials for Energy Storage, *Adv. Mater.*, 2017, **29**(20), 1601925, DOI: 10.1002/adma.201601925.

16 J. Hou, M. Hadouchi, L. Sui, J. Liu, M. Tang, Z. Hu, H. J. Lin, C. Y. Kuo, C. Te Chen, C. W. Pao, Y. Huang and J. Ma, Insights into Reversible Sodium Intercalation in a Novel Sodium-Deficient NASICON-Type Structure:$Na_{3.40}\square_{0.60}Co_{0.5}Fe_{0.5}V(PO_4)_3$, *Small*, 2023, **19**, DOI: 10.1002/smll.202302726.

17 F. Ahmad, A. Shahzad, S. Sarwar, H. Inam, U. Waqas, D. Pakulski, M. Bielejewski, S. Atiq, S. Amjad, M. Irfan, H. Khalid, M. Adnan and O. Gohar, Gel polymer electrolyte composites in sodium-ion batteries: synthesis methods, electrolyte formulations, and performance analysis, *J. Power Sources*, 2024, **619**, 235221, DOI: 10.1016/j.jpowsour.2024.235221.

18 M. Hadouchi, N. Yaqoob, P. Kaghazchi, M. Tang, J. Liu, P. Sang, Y. Fu, Y. Huang and J. Ma, Fast sodium intercalation in $Na_{3.41}£_{0.59}FeV(PO_4)_3$: a novel sodium-deficient NASICON cathode for sodium-ion batteries, *Energy Storage Mater.*, 2021, **35**, 192–202, DOI: 10.1016/j.ensm.2020.11.010.

19 J. Hou, M. Hadouchi, L. Sui, J. Liu, M. Tang, W. H. Kan, M. Avdeev, G. Zhong, Y. K. Liao, Y. H. Lai, Y. H. Chu, H. J. Lin, C. Te Chen, Z. Hu, Y. Huang and J. Ma, Unlocking fast and reversible sodium intercalation in NASICON $Na_4MnV(PO_4)_3$ by fluorine substitution, *Energy Storage Mater.*, 2021, **42**, 307–316, DOI: 10.1016/j.ensm.2021.07.040.

20 Y. Fang, L. Xiao, X. Ai, Y. Cao and H. Yang, Hierarchical Carbon Framework Wrapped $Na_3V_2(PO_4)_3$ as a Superior High-Rate and Extended Lifespan Cathode for Sodium-Ion Batteries, *Adv. Mater.*, 2015, **27**, 5895–5900, DOI: 10.1002/adma.201502018.

21 S. Sun, Y. Chen, Q. Bai, Z. Tian, Q. Huang, C. Liu, S. He, Y. Yang, Y. Wang and L. Guo, Unravelling the regulation mechanism of nanoflower shaped $Na_3V_2(PO_4)_3$ in methanol–water system for high performance sodium ion batteries, *Chem. Eng. J.*, 2023, **451**, 138780, DOI: 10.1016/j.cej.2022.138780.

22 X. Liao, X. Wu, M. Xie, X. Li, Y. Li, Z. Fu, G. Su, C. Fang, H. Zhang, Q. Zheng, J. Zhao, B. Xu and D. Lin, Leveraging high-entropy substitution to achieve $V^{4+}/V^{5+}$ redox couple and superior $Na^+$ storage in $Na_3V_2(PO_4)_3$-based cathodes for sodium-ion battery, *Energy Storage Mater.*, 2025, **77**, 104166, DOI: 10.1016/j.ensm.2025.104166.

23 S. Ghosh, N. Barman, M. Mazumder and S. K. Pati, High Capacity and High-Rate NASICON-$Na_{3.75}V_{1.25}Mn_{0.75}(PO_4)_3$ Cathode for Na-Ion Batteries *via* Modulating Electronic and Crystal Structures, *Adv. Energy Mater.*, 2019, **10**(6), 1902918, DOI: 10.1002/aenm.201902918.

24 M. V. Zakharkin, O. A. Drozhzhin, S. V. Ryazantsev, D. Chernyshov, M. A. Kirsanova, I. V. Mikheev, E. M. Pazhetnov, E. V. Antipov and K. J. Stevenson, Electrochemical properties and evolution of the phase transformation behavior in the NASICON-type $Na_{3+x}Mn_xV_{2-x}(PO_4)_3$ $(0 \leq x \leq 1)$ cathodes for Na-ion batteries, *J. Power Sources*, 2020, **470**, 228231, DOI: 10.1016/j.jpowsour.2020.228231.

25 J. Zhang, X. Zhao, Y. Song, Q. Li, Y. Liu, J. Chen and X. Xing, Understanding the superior sodium-ion storage in a novel $Na_{3.5}Mn_{0.5}V_{1.5}(PO_4)_3$ cathode, *Energy Storage Mater.*, 2019, **23**, 25–34, DOI: 10.1016/j.ensm.2019.05.041.

26 T. Long, P. Chen, B. Feng, C. Yang, K. Wang, Y. Wang, C. Chen, Y. Wang, R. Li, M. Wu, M. Lan, W. K. Pang, J. F. Wu and Y. L. Ding, Reinforced concrete-like $Na_{3.5}V_{1.5}Mn_{0.5}(PO_4)_3$@graphene hybrids with hierarchical porosity as durable and high-rate sodium-ion battery cathode, *Chin. Chem. Lett.*, 2024, **35**, 109267, DOI: 10.1016/j.cclet.2023.109267.

27 F. Lu, Y. Lu and L. Zhao, Dual carbon decorated $Na_{3.5}Mn_{0.5}V_{1.5}(PO_4)_3$ cathode with high-density and long-cycling span-life for sodium-ion batteries, *J. Power Sources*, 2025, **645**, 237194, DOI: 10.1016/j.jpowsour.2025.237194.

28 Y. Fan, Z. Peng, J. He, N. Sun, F. Ma, T. Zhang and F. Zhang, Simultaneous modification of $Na^+$-rich and $Mn^{2+}$-doping on $Na_3V_2(PO_4)_3$ for superior electrochemical performance: experimental and theoretical study, *J. Alloys Compd.*, 2025, **1010**, 177407, DOI: 10.1016/j.jallcom.2024.177407.

29 F. Chen, V. M. Kovrugin, R. David, O. Mentré, F. Fauth, J. N. Chotard and C. Masquelier, A NASICON-Type Positive Electrode for Na Batteries with High Energy Density: $Na_4MnV(PO_4)_3$, *Small Methods*, 2019, **3**, 1–9, DOI: 10.1002/smtd.201800218.

30 Y. Niu, Z. Yi, Y. Zhao and M. Xu, Synthesis and comparison of *in situ* carbon-decorated sodium manganese vanadium phosphate cathode and sodium-ion full-cell configurations, *Nano Sel.*, 2021, **2**, 1544–1553, DOI: 10.1002/nano.202000297.

31 M. Zhou, X. Zhou, L. Li, X. Chen, Z. Qiao and S. Chou, Emerging high voltage $V^{4+}/V^{5+}$ redox reactions in $Na_3V_2(PO_4)_3$-based cathodes for sodium-ion batteries, *Chem. Sci.*, 2024, **15**, 8651–8663, DOI: 10.1039/d4sc01226g.

32 S. Ghosh, N. Barman and P. Senguttuvan, Impact of $Mg^{2+}$ and $Al^{3+}$ Substitutions on the Structural and Electrochemical Properties of NASICON-$Na_xVMn_{0.75}M_{0.25}(PO_4)_3$ (M = Mg and Al) Cathodes for Sodium-Ion Batteries, *Small*, 2020, **16**, 1–8, DOI: 10.1002/smll.202003973.

33 X. Zhang, H. Mao, Z. Chen, L. Zhou, L. Liu, M. Wu, Z. Lv, Z. Zhang, Y. Zhong and Y.-S. Hu, Rational Design of Phosphate Cathodes with Improved Na-storage Performance, *ACS Energy Lett.*, 2025, **10**, 2804–2810, DOI: 10.1021/ACSENERGYLETT.5C00653.

34 L. Chayal, S. El Arni, M. Saadi, A. Assani, L. Bih, J. Ma and M. Hadouchi, Insights into structure, morphology and conductivity of the earth-abundant NASICON phosphate, $Na_4MnFe(PO_4)_3$, *RSC Adv.*, 2024, **14**, 22159–22168, DOI: 10.1039/d4ra03529a.

35 Y. Zhu, H. Xu, Y. Bao, S. Li and Y. Chen, Ternary NASICON-Type $Na_{3.25}VMn_{0.25}Fe_{0.75}(PO_4)_3$/NC@CNTs Cathode with Reversible Multielectron Reaction and Long Life for Na-Ion Batteries, *ACS Appl. Mater. Interfaces*, 2025, **17**, 7581–7594, DOI: 10.1021/acsami.4c15767.

36 C. Xu, J. Zhao, E. Wang, X. Liu, X. Shen, X. Rong, Q. Zheng, G. Ren, N. Zhang, X. Liu, X. Guo, C. Yang, H. Liu, B. Zhong and Y. S. Hu, A Novel NASICON-Typed $Na_4VMn_{0.5}Fe_{0.5}(PO_4)_3$ Cathode for High-Performance Na-Ion Batteries, *Adv. Energy Mater.*, 2021, **11**, 1–9, DOI: 10.1002/aenm.202100729.

37 P. X. Xie, Q. Y. Zhao, H. Dong, T. Long, M. S. Ding, B. Xie, X. F. Wang, W. Ling, M. Liu, X. W. Wu, P. F. Wang and X. X. Zeng, Reversible $V^{4+}/V^{5+}$ redox in $Na_4VFe(PO_4)_3$ cathode for high-power sodium-ion batteries, *Chem. Eng. J.*, 2025, **509**, 161209, DOI: 10.1016/j.cej.2025.161209.

38 C. Xu, R. Xiao, J. Zhao, F. Ding, Y. Yang, X. Rong, X. Guo, C. Yang, H. Liu, B. Zhong and Y. S. Hu, Mn-Rich Phosphate Cathodes for Na-Ion Batteries with Superior Rate Performance, *ACS Energy Lett.*, 2022, **7**, 97–107, DOI: 10.1021/acsenergylett.1c02107.

39 J. Rodriguez-Carvajal, FULLPROF: a program for Rietveld refinement and pattern matching analysis, in *Satell. Meet. Powder Diffr. XV Congr. IUCr*, Toulouse, France, 1990, p. 127.

40 K. Brandenburg and H. Putz, Diamond-crystal and molecular structure visualization crystal impact, *Rathausgasse*, 2006, **30**, 1997–2000.

41 W. Duan, Z. Zhu, H. Li, Z. Hu, K. Zhang, F. Cheng and J. Chen, $Na_3V_2(PO_4)_3$@C core-shell nanocomposites for rechargeable sodium-ion batteries, *J. Mater. Chem. A*, 2014, **2**, 8668–8675, DOI: 10.1039/c4ta00106k.

42 I. D. Brown and D. Altermatt, Bond-valence parameters obtained from a systematic analysis of the inorganic crystal structure database, *Struct. Sci.*, 1985, **41**, 244–247, DOI: 10.1107/S0108768185002063.

43 H. Guonie, C. Shi, C. Chen and C. Shang, High-performance $Na_{3.5}Fe_{0.5}V_{1.5}(PO_4)_3$ cathodes enabled by phase control and CQD-containing carbon coating, *J. Mater. Chem. A*, 2025, **13**, 37631–37640, DOI: 10.1039/d5ta06954h.

44 Y. L. Ruan, K. Wang, S. D. Song, X. Han and B. W. Cheng, Graphene modified sodium vanadium fluorophosphate as a high voltage cathode material for sodium ion batteries, *Electrochim. Acta*, 2015, **160**, 330–336, DOI: 10.1016/j.electacta.2015.01.186.

45 V. S. Kurazhkovskaya, D. M. Bykov and A. I. Orlova, Infrared spectroscopy and structure of trigonal zirconium orthophosphates with lanthanides and actinides, *J. Struct. Chem.*, 2004, **45**, 966–973, DOI: 10.1007/s10947-005-0087-5.

46 Z. Jian, W. Han, X. Lu, H. Yang, Y. S. Hu, J. Zhou, Z. Zhou, J. Li, W. Chen, D. Chen and L. Chen, Superior electrochemical performance and storage mechanism of $Na_3V_2(PO_4)_3$ cathode for room-temperature sodium-ion batteries, *Adv. Energy Mater.*, 2013, **3**, 156–160, DOI: 10.1002/aenm.201200558.

47 I. Obraztsov, A. Cymann-sachajdak, K. Bruniecka, P. Madajski, S. Veronika, G. Trykowski, A. Bakandritsos and M. Wilamowska-zawłocka, Densely Carboxylated Graphene for Synthesis of High-Performing NASICON Cathodes for Na-Ion Batteries, *ACS Appl. Mater. Interfaces*, 2026, **18**(3), 5279–5289, DOI: 10.1021/acsami.5c21272.

48 R. Enggar, A. Ardhi, G. Liu and X. M. Tran, Self-Relaxant Super-Elastic Matrix Derived from C 60 Incorporated Sn Nanoparticles for Ultra-High- Performance Li-Ion Batteries, *ACS Nano*, 2018, **12**(6), 5588–5604, DOI: 10.1021/acsnano.8b01345.

49 A. Kim, R. Enggar, A. Ardhi, G. Liu, J. Young, H. Shin, D. Byun and J. Kee, Hierarchical hollow dual core–shell carbon nanowall-encapsulated p–n $SnO/SnO_2$ heterostructured anode for high-performance lithium-ion-based energy storage, *Carbon*, 2019, **153**, 62–72, DOI: 10.1016/j.carbon.2019.07.001.

50 S. Chen, J. Hou, X. He, Q. Wang, W. Wang, M. Zhou, K. Wang and K. Jiang, Enhancing the Sodium Storage Performance of $Na_4MnCr(PO_4)_3$ through the Manipulation of Intrinsic Site Occupation Defects, *ACS Appl. Mater. Interfaces*, 2024, **16**, 52653–52662, DOI: 10.1021/acsami.4c10821.

51 M. T. Ahsan, Z. Wu, Y. Liu, H. Chen, M. Li and D. Li, Unlocking the Ultrastable Sodium Storage *via* Cation Engineering in Vanadium-Iron-Based NASICON Framework, **04885**, 2025, 1–12, DOI: 10.1002/aenm.202504885.

52 Y. Chen, Q. Li, P. Wang, X. Liao, J. Chen, X. Zhang, Q. Zheng, D. Lin and K. Lam, High-Energy-Density Cathode Achieved *via* the Activation of a Three-Electron Reaction in Sodium Manganese Vanadium Phosphate for Sodium-Ion Batteries, **2**, 2023, 3–11, DOI: 10.1002/smll.202304002.

53 M. T. Ahsan, Z. Ali, J. Wang, W. Zhao and Y.-L. Hou, Robust sodium storage enabled medium entropy $Na_{3.5}V_{0.5}Mn_{0.5}Fe_{0.5}Ti_{0.5}(PO_4)_3$ NASICON with multielectron reaction for sodium-ion battery, 2025, 2328–2339, DOI: 10.1007/s12598-024-03009-9.

54 F. Lalère, V. Seznec, M. Courty, R. David, J. N. Chotard and C. Masquelier, Improving the energy density of $Na_3V_2(PO_4)_3$-based positive electrodes through V/Al substitution, *J. Mater. Chem. A*, 2015, **3**, 16198–16205.

55 K. Lin, M. Liu, X. Qin, G. Zheng, J. Liang, B. Li and C. Jiang, Practical Evaluation of Presodiation Techniques for High Energy Sodium-Based Batteries, *ACS Nano*, 2025, **19**(18), 17062–17086, DOI: 10.1021/acsnano.5c02104.

56 M. Xu, F. Zhang, Y. Zhang, C. Wu, X. Zhou, X. Ai and J. Qian, Chemical Science Controllable synthesis of a Na-enriched sodiation approach, 2023, 12570–12581, DOI: 10.1039/d3sc03498d.

57 Y. Liu, L. Zhu, E. Wang, Y. An, Y. Liu, K. Shen and M. He, Electrolyte Engineering with Tamed Electrode Interphases for High-Voltage Sodium-Ion Batteries, 2024, 1–12, DOI: 10.1002/adma.202310051.

58 M. Sharma and R. S. Dhaka, Electrochemical Performance and Diffusion Kinetics of a NASICON type $Na_{3.3}Mn_{1.2}Ti_{0.75}Mo_{0.05}(PO_4)_3$/C Cathode for Low-Cost Sodium-Ion Batteries, *Small*, 2025, 2505200, DOI: 10.1002/smll.202505200.

59 M. Chen, W. Hua, J. Xiao, D. Cortie, W. Chen, E. Wang, Z. Hu, Q. Gu, X. Wang, S. Indris, S. Chou and S. Dou, NASICON-type air-stable and all-climate cathode for sodium-ion batteries with low cost and high-power density, *Nat. Commun.*, 2019, **10**, 1480, DOI: 10.1038/s41467-019-09170-5.

60 D. Liu, J. Guo, Y. Sun and X. Zhang, NASICON-structured $Na_3Mn_{0.5}V_{0.5}Ti(PO_4)_3$ cathode with high capacity for sodium-ion batteries, *Ceram. Int.*, 2022, **48**, 20933–20939, DOI: 10.1016/j.ceramint.2022.04.085.

61 W. Choi, H.-C. Shin, J. M. Kim, J.-Y. Choi and W.-S. Yoon, Modeling and applications of electrochemical impedance spectroscopy (EIS) for lithium-ion batteries, *J. Electrochem. Sci. Technol.*, 2020, **11**, 1–13, DOI: 10.33961/jecst.2019.00528.

62 T. S. Sahu and S. Mitra, Exfoliated $MoS_2$ Sheets and Reduced Graphene Oxide-An Excellent and Fast Anode for Sodium-ion Battery, *Sci. Rep.*, 2015, **5**, 1–13, DOI: 10.1038/srep12571.

63 T. Yang, L. Sang, F. Ding, J. Zhang and X. Liu, Three- and four-electrode EIS analysis of water stable lithium electrode with solid electrolyte plate, *Electrochim. Acta*, 2012, **81**, 179–185, DOI: 10.1016/j.electacta.2012.07.103.

64 S. She, Y. Zhou, Z. Hong, Y. Huang and Y. Wu, Effect of Fluoroethylene Carbonate Electrolyte Additives on the Electrochemical Performance of Nickel-Rich NCM Ternary Cathodes, *ACS Appl. Energy Mater.*, 2023, **6**, 7289–7297, DOI: 10.1021/acsaem.3c01025.